Lawrence Berkeley National Laboratory

Title
Nanometer-scale imaging and pore-scale fluid flow modeling in chalk

Permalink
https://escholarship.org/uc/item/8d3009q2

Authors
Tomutsa, Liviu
Silin, Dmitriy
Radmilovich, Velimir

Publication Date
2005-08-23

Peer reviewed

NANOMETER-SCALE IMAGING AND PORE-SCALE FLUID FLOW MODELING IN CHALK

LIVIU TOMUTSA (SPE), DMITRIY SILIN (SPE) AND VELIMIR RADMILOVIC

Lawrence Berkeley National Laboratory, Berkeley, CA, U.S.A.

ABSTRACT

For many rocks of high economic interest such as chalk, diatomite, tight gas sands or coal, nanometer scale resolution is needed to resolve the 3D-pore structure, which controls the flow and trapping of fluids in the rocks. Such resolutions cannot be achieved with existing tomographic technologies. A new 3D imaging method, based on serial sectioning and using the Focused Ion Beam (FIB) technology has been developed. FIB allows for the milling of layers as thin as 10 nanometers by using accelerated Ga+ ions to sputter atoms from the sample surface. After each milling step, as a new surface is exposed, a 2D image of this surface is generated. Next, the 2D images are stacked to reconstruct the 3D pore or grain structure. Resolutions as high as 10 nm are achievable using this technique. A new image processing method uses direct morphological analysis of the pore space to characterize the petrophysical properties of diverse formations. In addition to estimation of the petrophysical properties (porosity, permeability, relative permeability and capillary pressures), the method is used for simulation of fluid displacement processes, such as those encountered in various improved oil recovery (IOR) approaches. Computed with the new method capillary pressure curves are in good agreement with laboratory data. The method has also been applied for visualization of the fluid distribution at various saturations from the new FIB data.

INTRODUCTION

Field-scale oil recovery processes are result of countless events happening in individual pores. To model multiphase flow in porous media at pore scale, 3D data are needed with a resolution adequate for the rock of interest. Chalk formations are encountered in oil fields in the Texas, Middle East, North Sea, etc. Chalk reservoirs hold significant oil reserves. The extremely small typical pore sizes in chalk impose very high requirement on imaging resolution. In the last decade, X-ray microtomography has been used extensively for direct visualization of pore system and the fluids within sandstone (Jasty, J.K. *et al*, 1993, Coles *et al*, 1996, Wildenschild *et al*, 2002*,* Seright *et al*, 2003). While this approach is relatively fast and nondestructive, its applicability is mostly limited to micron resolutions, although recent developments are bringing the resolution to submicron range (Stampanoni *et al*, 2002). For chalk pore systems, which are characterized by submicron to nanometer length scales, 3D stochastic methods based on 2D scanning electron microscope (SEM) images of thin sections have been used to reconstruct the pore system (Talkudar *et al*, 2001). The advent of the Focused Ion Beam technology has made it possible to reconstruct submicron 3D pore systems. 2D and 3D images for diatomite and chalk pore structures are shown in Figure 1. (Tomutsa and Radmilovic, 2003). FIB technology is used in microelectronics to access individual components with nanoscale accuracy for design verification, failure analysis and circuit modification (Orloff *et al*, 2002). It also has been used in material sciences for sectional sample preparation for SEM and for 3D imaging of alloys components (Kubis *et al*, 2004). In earth sciences, FIB has been used for sample preparation for SEM and to access inner regions for performing microanalysis (Heaney *et al*, 2001). To access the pore structure at submicron scale, FIB mills successive layers of the rock material as thin as 10 nm. As successive 2D surfaces are exposed, they are imaged using either the electron or the ion beam. After processing, the images are stacked to reconstruct the 3D pore structure. To analyze the 3D chalk images obtained by the FIB method, we applied a recently developed technique (Silin *et al.*, 2003). A distinctive feature of this approach is that the 3D pore space image is analyzed directly, without construction of pore networks. This approach bypasses the nontrivial task of extracting a simple but representative network of pore throats linking pore bodies from the 3D data (Lindquist, 2002). Moreover, the pore network extraction methods based on relatively simple grain shapes in sandstones, (Øren and Bakke, 2002) may be not always feasible for the complex pore structures of carbonates. Although pore-network based flow

modeling approach enjoyed a significant interest from the researchers and resulted in theoretically and practically sound conclusions (Øren *et al.*, 1998; Patzek, 2001; Blunt, 2001), we feel that direct pore space analysis deserves more attention. In addition, direct analysis of the pore space provides an opportunity to study alteration of the rock flow properties, *e.g.*, due to mechanical transformations or mineralization (Jin *et al.*, 2004).
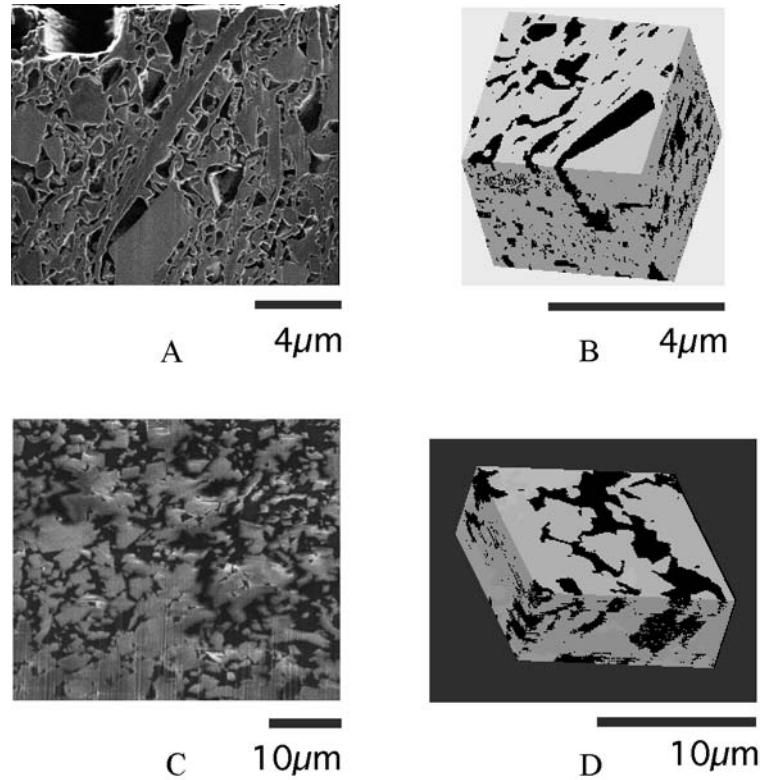

Figure 1. FIB images of diatomite(A) and chalk (C) and 3D reconstructions (B,D)

EXPERIMENTAL

Equipment

The FIB apparatus used in this study is model FEI Strata DB235, dual electron and ion beam. It is a scanning electron microscope (SEM) that has also the capability to focus gallium ions (Ga+) accelerated by potentials up to 30kV. Both, secondary electrons and secondary ions can be used for imaging and the digitized images are stored in 1024×954, 8 bit, TIF format. The image contrast is determined both by the topography of the sample and by the difference in the atomic numbers of the materials present at the sample surface. Thus, a good pore/grain contrast can be achieved for both epoxy-impregnated and nonimpregnated samples. To avoid damaging the sample by the ion beam during imaging, a low beam current (10-100 pA) and/or a short imaging time (seconds) are recommended. During milling, the ion beam current can be increased by orders of magnitude (up to 20,000 pA) and the exposure time can be increased up to hours. An important feature of the instrument is a 5-axis computer-controlled stage, which allows for repeatable access to the same location on the sample surface. The stage allows for the sample orientation either normal to the ion beam for drilling submicron scale patterns, or quasi parallel for milling successive layers. The large sample chamber and the number of

ports present allows for installation of various other instruments (element analysis, platinum deposition, micromanipulator, *etc.*) (Fig**.** 2).

Figure 2. FIB Sample chamber with sample mounted on 45 deg stage

Methodology

To perform 3D imaging using FIB technology, the samples are prepared using standard SEM procedures, *i.e.* cleaning, cutting, polishing, mounting and carbon coating. Good sample cleaning is important to minimize hydrocarbon contamination of the instrument and interference with the high vacuum. Because the FIB mills submicron layers, the sample surface has to be flat at the micron scale. High roughness of the sample surface can significantly increase the time required for the FIB to mill the surface to the flatness required for serial sectioning. For soft materials, such as diatomite, a microtome can be used while for harder materials or epoxy impregnated samples, diamond saw cutting and standard thin section procedures for polishing is recommended. The prepared sample is mounted on a 45 degrees SEM stub using conducting adhesive (Fig. 3). As seen in Figure 3, ion milling and SEM imaging can be performed without moving the sample, except for minor refocusing. The SEM approach is the preferred mode of operation from the point of view of increased productivity and improved registration of images if there is a good contrast between the pore space and the matrix, and the charge build up on the sample is not too rapid. The ion beam imaging yields better quality images than the electron beam imaging, due to less charging of the surface, but it is significantly more time consuming to implement due to sample repositioning and refocusing between the milling and imaging steps. Once the region to be milled has been defined (Fig. 4), the depth milled is proportional with the time elapsed. Thus, images captured at equal time intervals display equidistant surfaces at increasing depths within the sample volume. The time required to mill a certain quantity of material depends on the ion current and the sample material. For example, the time required to mill a volume $50 \times 50 \times 0.1$ μm in chalk is of the order of minutes, for 30 kV, 3000 pA Ga+ ions beam. Higher currents (7000-20,000 pA) will cut faster, but also will yield rougher surfaces, and negatively affect the image quality.

Very clean flat surfaces, in which the pore-grain boundaries appear in high contrast, can be generated with no apparent distortion of the pore boundaries. The pore/matrix contrast is more pronounced in an epoxy-impregnated sample than in samples not impregnated. After each milling episode, images are acquired at a selected magnification such that each view captures the desired number of pores with the adequate resolution.

3

Next, the individual 2D images are stacked and aligned using registration (fiduciary) markings or characteristic features within the sample volume. The segmentation of the data into pore/nonpore voxels can be performed either on the 2D images or on the 3D data sets. For images with high pore/nonpore gray scale contrast, simple thresholding could be adequate (Fig. 5). For lower-contrast images, which can benefit from using spatial information besides gray level, other methods, such as indicator krigging are available (Oh and Lindquist, 1999, Mardia-Hainsworth, 1988, Lindquist (2002). To process the images,especially for batch image manipulation and segmentation, commercial image processing software package (such as ImagePro or NOESYS, etc..) or freeware (such as Image-J, www.nih.gov/ij or 3DMA, www.ams.sunysb.edu/~lindquis/3dma/3dma`rock.html) can be used. In this work Image J and NOESYS packages were used.
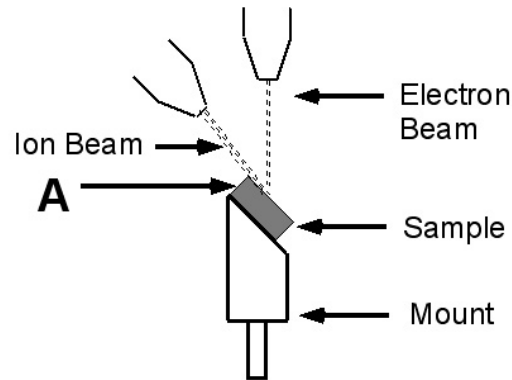

Figure 3. Sample mounted for FIB milling and imaging.

Figure 4. View from the ion beam direction of sample surface **A** during milling. The milling boundary is

defined by the white rectangle and the most recent surface exposed is marked by the middle horizontal segment
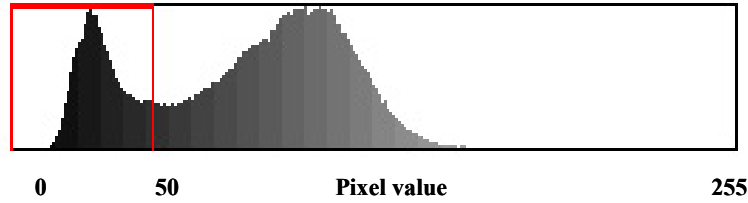
Figure 5. Histogram displaying a high pore/grain contrast. Pore pixel values in 0-50 interval.

Experimental Results

The sample studied, courtesy of ConocoPhillips, was a 1 in diameter Ekofisk plug with 29% He porosity and permeability of 4 md. The sample was CT scanned using a Somatom HiQ medical CT scanner(1mm thick slices, 133 kV, 120 mA) and a porosity distribution was determined. As seen in the four representative crossections shown in Figure 6, the sample has a uniform porosity, except for a few mm-scale low porosity regions apparent both on CT and visually. The mean CT measured porosity is 29% and in the low porosity regions is 25%. The 6×4×2 mm sample selected for imaging was from a region with 29% porosity. The sample was epoxy impregnated under vacuum, followed by up to 1400 psi pressure. It was polished following standard thin section preparation techniques using up to 1 µm size diamond polishing disk. The chalk sample presented a good contrast between the epoxy-filled pore space and the matrix, which allowed for secondary electron imaging (SED detector) at 5 kV electron energy by using a 12 s scan, with minimal charging taking place (Fig. 7). The pixel resolution was 0.05 µm. The sections imaged were spaced 0.1 µm apart. To create 0.05 µm cubic voxels, the number of 2D images was doubled by using interpolation between consecutive layers by a spline-based algorithm TransformJ (Meijering, 2001). The good contrast allowed for direct thresholding of the layers to generate a 3D binary image using ImageJ package. A 3D reconstruction of a subset of the binary data is shown in Figure 8.
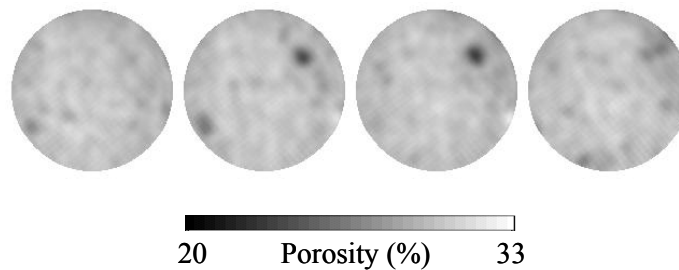
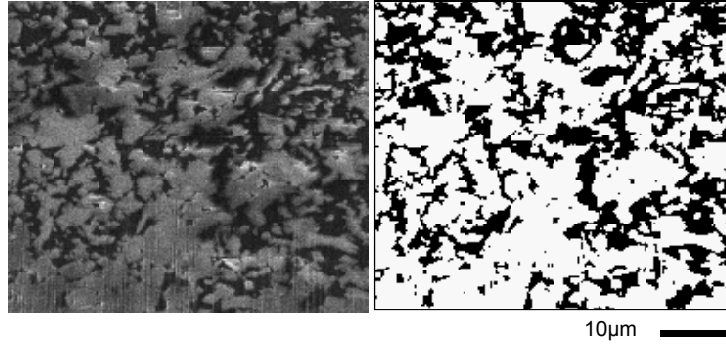

Figure 6. CT derived porosity crossections of chalk plug

10μm

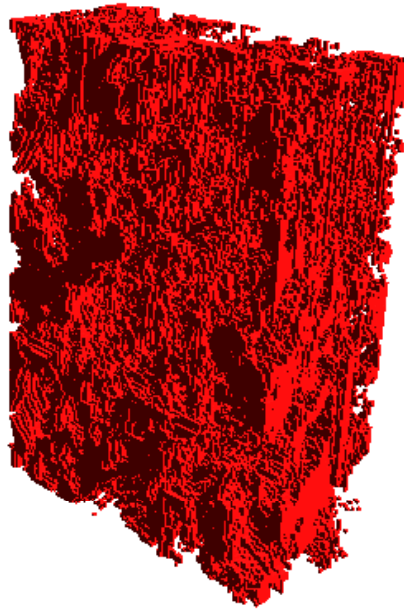Figure 7. SEM image of FIB prepared surface, before (left) and after segmentation (right)

Figure 8. 3D pore reconstruction of $22\times32\times10$ μm^3 ($200\times450\times636$ voxels)chalk volume

PORE SPACE ANALYSIS

The acquired FIB images are processed for estimating rock properties, which determine the IOR operations. The method used in this study is based on the concept of a maximal inscribed ball, or sphere (MIS). It is a light version of the algorithms described in Silin *et al*., 2003, 2004. A similar approach was applied to analyze statistically reconstructed media by Magnani *et al.*, 2000. The principle idea is to compute the part of the pore space occupied by wetting and non-wetting fluid, respectively, based on Young-Laplace equation. According to this equation, the curvature of the interface between two immiscible fluids is determined by the capillary pressure. Such an interface, in turn, can be approximated by a spherical surface of the corresponding radius. Therefore, at a given capillary pressure, the part of the pore space occupied by the non-wetting fluid can be approximately represented as the union of all balls of this radius, which can be inscribed into the pore space. An extended set of rules can be applied to model a mixed wettability environment and/or nonzero contact angle.

As any numerical procedure, the maximal inscribed spheres method (MIS-calculation) presents only an approximate picture of the distribution of the fluids. Besides imaging resolution and discretizarion limitations, there are several sources of possible inaccuracies imposed by the method itself. For instance, not always the shape of the fluid-fluid interface is perfectly spherical. The curvature of the union of spheres of a given radius, in general, is different from the curvatures of the individual spheres. However, examples below demonstrate remarkable agreement between the results of computations and laboratory experiments. This agreement shows that the assumption of spherical interface introduces noticeable errors into volume estimations mostly locally. Most probably, these local errors are larger near to the pore walls, whereas in the central parts of the pores, the MIS-description as adequate enough. Note that the typical length scale of the chalk pores is in tens or hundreds of nanometers. So the fact that the near-wall boundary effects did not significantly spoil the results of computations is very encouraging.

An input to MIS-calculation is a digitized image after segmentation, *i.e.* a cube of voxels, each one of which is assigned either zero or one, depending whether the voxel center is in the solid phase or in the pore space. In this study, the images were obtained using FIB technology described above. Naturally, segmentation of a raw image can produce artifacts in the form of several pore-space voxels inside the solid phase, and, *vice versa*, solid voxels "suspended" in the pore space. Although visually such artifacts may be hardly noticeable, they can significantly interfere in the MIS-calculations. Therefore, to eliminate imaging and segmentation errors and artifacts, prior to any further computations, the data set is first "cleaned" by removing small isolated clusters of solid phase inside pores and small isolated pores inside the solid phase. Cluster search algorithms (Silin and Patzek, 2003) were adjusted and customized in order to handle a 3D pore space image, rather than a pore network. To check, whether the cluster of voxels is isolated or not, different connectivity rules can be applied: 6-connectivity, where two voxels are connected if they have a common face, 18-connectivity, where two voxels are connected if they have a common edge, and 26-connectivity, where a common vertex between two voxels implies connection. If two voxels are connected according to the first rule, they are connected according to the second and third ones as well; 18-connectivity implies 26-connectivity. In the elimination of the isolated pores and "solid dust", the 6-connectivity was applied. This strict rule turned out to be most efficient for a cleanup operation because otherwise imaging artifacts like narrow branches of voxels protruding into the pores significantly perturbed occupation and invasion rules in the percolation simulations.

After the preliminary cleaning, the following two major steps are performed as parts of the numeric MIS-calculations procedure. First, for each voxel, the squared radius of the largest ball centered at this voxels is computed. The lengths in computations are scaled with voxel size, so voxel coordinates are integer numbers. Therefore, the use of squared radii makes it possible to operate with integer variables only. This simple trick reduces the complexity of computations and eliminates round-off errors. Second, each pore voxel is assigned a value equal to the maximal squared radius of a ball included in the pore space and including this voxel. Once such a three-dimensional table is setup, various types of analysis can be performed using scanning algorithms and by grouping voxels into clusters with specific properties. In fact, to make the algorithm more efficient, this table is accompanied by a list of pore voxel. In invasion percolation simulations, 18-connectivity rule was applied. The nonwetting fluid connectivity also was verified using the 18-connectivity rule. This rule was selected because it yields clusters of voxels most appropriate for fluid flow simulations using the lattice-Boltzmann or other methods.

The entire image represents just a tiny fragment cut from the formation. Therefore, the imaged portion (or portions) of a pore at the image boundary provides little or no information about the size and shape of the entire pore. To handle this uncertainty, in this study, a convention has been adopted that the pore space structure is mirror-reflected over the image-boundary plane.

Assigning to each voxel the maximal squared radius of a ball, which is inside the pore space and which covers this voxel, is an auxiliary procedure from the point of view of the main objectives of the study. However, it produces very important information about the pore space structure and is the starting point for all other computations. To see how this information can be generated, let us consider a simple two-dimensional illustrative example. An ellipsoid is discretized and segmented into a set of pixels, Figure 9. For each pixel, the squared radius of the maximal discrete circle inscribed in the pore space and centered at this pixel is evaluated.

The result is displayed on the left-hand picture. However, after assigning to each pixel the squared radius of the maximal covering disk, the picture is different, Figure 9 on the right. Almost all pixels in the ellipsoidal "pore" have the same number. The centers of the two maximal (discrete) disks of the maximal radii are in boldface typeset. In particular, this example shows that a larger pore opening, a pore body, is associated with a cluster of voxels covered by locally-maximal inscribed spheres. In this particular example, the voxels assigned with smaller radii (voxels marked by 2 on the right-hand picture) are not associated with pore space corners or crevices, but are significantly outnumbered.
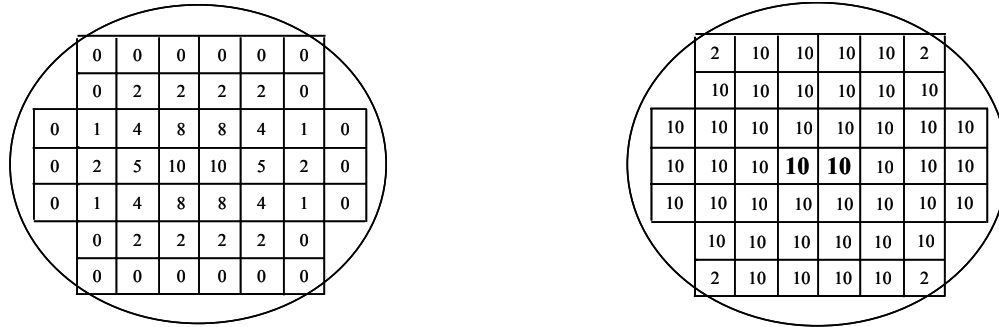

Figure 9. Digitized ellipsoid. The left-hand picture displays maximal squared radii of the discrete circles contained in the pore space and centered at each voxel. The right-hand picture displays maximal squared radii of the covering disks. The highlighted voxels are the centers of those disks.

The distribution of the counts of voxels with given MIS radii can be used as statistical parameter characterizing pore space geometry. Figure 10 presents the bar plot of squared radii distribution in the 200×636×450 voxels image of chalk and, a similar distribution for a 400×400×400 CT image of Fontainebleau sandstone (the latter is courtesy of Schlumberger). Note that the resolution for the chalk data is two orders of magnitude higher than that for the sandstone. The bars corresponding to the smallest radii have been removed from the chalk diagram in order to present both plots in comparable scales. The bar corresponding to the smallest radius was cut for sensible scaling of the "spectral decomposition" of the pore space in Figure 10. The plots highlight the differences in the pore space geometries of the two types of rock as well as some features of the imaging technique. The presence of isolated peaks indicates the presence of a few relatively large pores in chalk, which is one of its distinguishing features. The radii distribution of sandstone is more uniform. The latter fact has a noticeable impact on the shape of the capillary pressure curve, as described below. FIB technique described above requires stacking of multiple images, Figure 3. Microscopic misalignments of the layers may create numerous small corners. Therefore, the large number of single-voxel "corners" in the chalk image could be partially explained by slight misalignement of individual 2D images.

The squared radii table was used to simulate equilibrium fluid distribution in the pore space at different capillary pressures. The dimensionless capillary pressure curve provides information about the pore space geometry and characteristic dimensions of the pores. It plays a role, which is similar to the spectral decomposition described above. Different types of rock are, in particular, characterized by different curves.

To test the sample for heterogeneity and to assess the impact of the image resolution on the output, the 200×450×636 data set was split into cubic parts of dimensions 200×200×200. The dimensionless capillary pressure curves were plotted at different resolutions and for different fragments of the same image. Since not all image dimensions are divisible by 200, some parts overlapped each other. For each fragment, the squared radii distribution and the dimensionless capillary pressure curve were calculated. The left plot in Figure 11 shows all the radii squared distributions plotted in the same coordinate axes. A comparison of this plot to a similar plot for the entire image, Figure 10, suggests that the general structure of larger pores is preserved and

the subimages are fairly representative. However, since some pores can be cut into parts by partitioning the entire image, the distribution can be distorted.
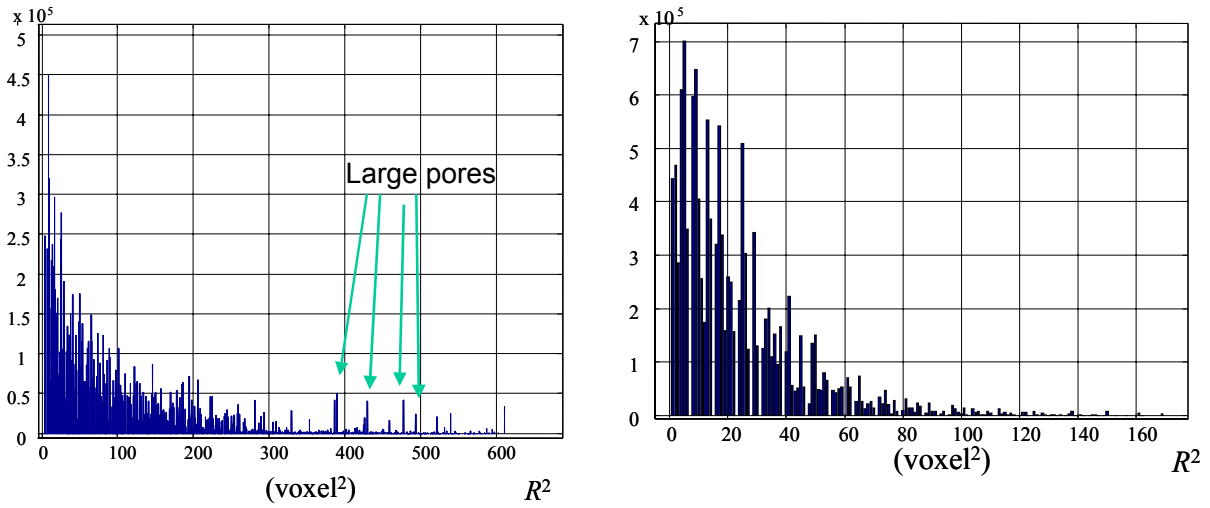

Figure 10. "Spectral analysis" of the pore space. Maximal radii distribution indicating presence of several large pores in the images of chalk plug (left-hand picture) and more uniform decay of the distribution of the pore sizes of Fontainebleau sandstone (right-hand side picture Note that the resolution of the chalk image 0.05μm and for sandstone is 5μm/voxel.
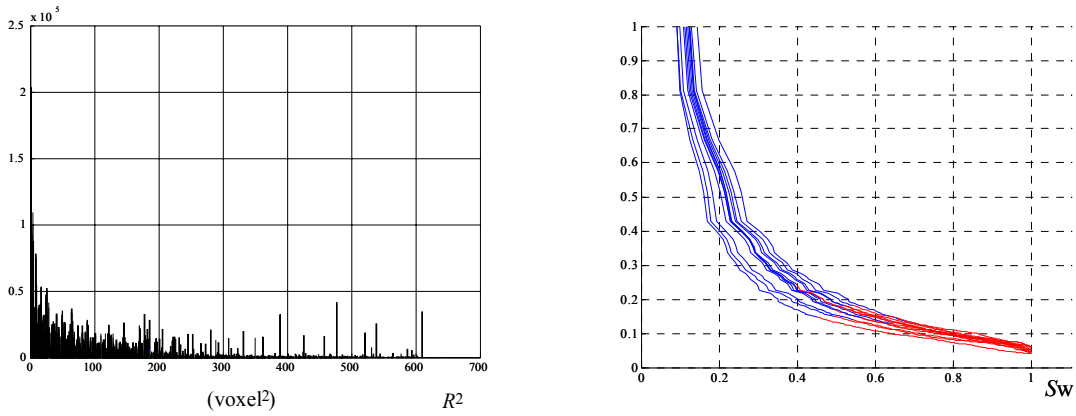

Figure 11. Squared radii distribution and dimensionless capillary pressure curves for twelve different 200×200×200 voxels fragments. The difference between the curves indicates heterogeneity of the sample.

Comparison among dimensionless capillary pressure curves corresponding to the different parts of the image (the right-hand side plot in Figure 11) indicates significant heterogeneity. Indication of such heterogeneity is noticeable in the radii distribution plot as well, Figure 11, on the left. Due to the presence of several relatively large pores, the fragments, which include those pores, have larger porosity and show lower capillary pressures. Apparently, the two separate curves in the right-hand side plot in Figure 11, lying below the other curves, correspond to such fragments. In contrast, the dimensionless capillary pressure curves for Fontainebleau sandstone practically collapsed in a similar analysis (Silin *et al.*, 2003). Therefore, the local heterogeneity of sandstone is much lower than that of chalk.

9

The dimensionless capillary pressure curves have been calculated based on simple percolation and do not account for the history of fluid migration. Implicitly, it is assumed that the pore space is initially saturated with a nonwetting fluid. The wetting fluid can always reach to all pores along the corners and surface roughness. As capillary pressure increases, the nonewetting fluid is displaced as long as it preserves its connectivity. In the simulations described here this connectivity was preserved on a wide range of wetting fluid saturations. Therefore, simple percolation better simulates the imbibition capillary pressures curves rather than those of primary drainage. Once the nonwetting fluid becomes disconnected and is trapped, its flow practically stops. Therefore, only those parts of the presented curves, which correspond to connected non-wetting fluid, are physically sensible. Computation of the connectivity threshold is a part of the applied percolation algorithm. The predicted loss of connectivity at 50-70% saturation is in good agreement with experimental results reported for an Ekofisk chalk sample with similar petrophysical properties (Spinler and Baldwin, 1997, Figures 14 and 17). In present work, the simulations account for positive capillary pressures only, which correspond to spontaneous equilibrium fluid distribution. Since spontaneous imbibition is intrinsically a non-equilibrium process, dynamic simulations of such a process require certain modifications of the steady-state capillary pressure curves (Barenblatt *et al.*, 2003; Silin and Partzek, 2004).

At any given radius squared, that is, at any given capillary pressure, the algorithm finds all clusters occupied by the wetting and nonwetting fluid, analyzes the connectedness of the clusters, and seeks clusters spanning between the inlet and outlet faces. The fluid distribution can be visualized in order to observe how the fluids "displace" one another. In addition, sequences of such images provide information about the 3D structure of the pore space, which is practically impossible to obtain just by analyzing two-dimensional cross-sections. In Figure 12, the fluid configurations are displayed at several saturations in a $100 \times 100 \times 100$ voxels fragment of the image. It is noticeable that the nonwetting fluid gets disconnected at a low wetting fluid saturation, which is lower than the typical 50-70% saturation obtained for larger images. This can be related to the fact that some flow paths have a very complex geometry and pass across several adjacent parts of such size.

To scale the capillary curves, computations on a sample with dimensions $10 \times 22.5 \times 32.8$ μm and its middle part $5 \times 22.5 \times 32.8$ μm were performed. The difference in the size of the image in different directions is implied by the FIB imaging method. For each direction, it was assumed that the sample is open only in this direction and sealed at all other faces. Also, additional simulations were performed under the assumption that all the faces of the sample were open for the flow. Invasion percolation simulations were carried out using cluster search algorithms (Silin and Patzek, 2003) adjusted for 3D voxel image analysis. The image of the same core sample was taken at three different resolutions: 0.05 μm, 0.1 μm and 0.2 μm. It was assumed that the surface tension coefficient between the fluids is equal to 20 dynes/cm that is a reasonable value for water-oil interface (Muskat, 1949). The computed scaled capillary pressure curves are gathered in Figures 13 and 14 (solid lines). The plots show that for large wetting fluid saturations and low capillary pressures the results are consistent for all three resolutions. However, at lower saturations and, respectively, higher capillary pressures, the 0.2 μm resolution is too coarse. The shapes of invasion-percolation curves and the absolute values of capillary pressures are in agreement with the drainage capillary pressure curve reported in Spinler and Baldwin, 1997. The presence of relatively large pores results in almost horizontal segments of invasion-percolation capillary pressure curves. Indeed, to pass a "bottleneck" leading into a larger opening, the capillary pressure needs to reach a certain threshold value, the entry capillary pressure. Once this pressure has been reached, the nonwetting fluid fills the large pore and the local saturation changes abruptly. The shape and the capillary pressure values computed form simple percolation curves resemble those of the imbibition curve, Figure 15. In all cases, the agreement between computed and experimental curves is better at saturations, for which the nonwetting fluid is still connected.
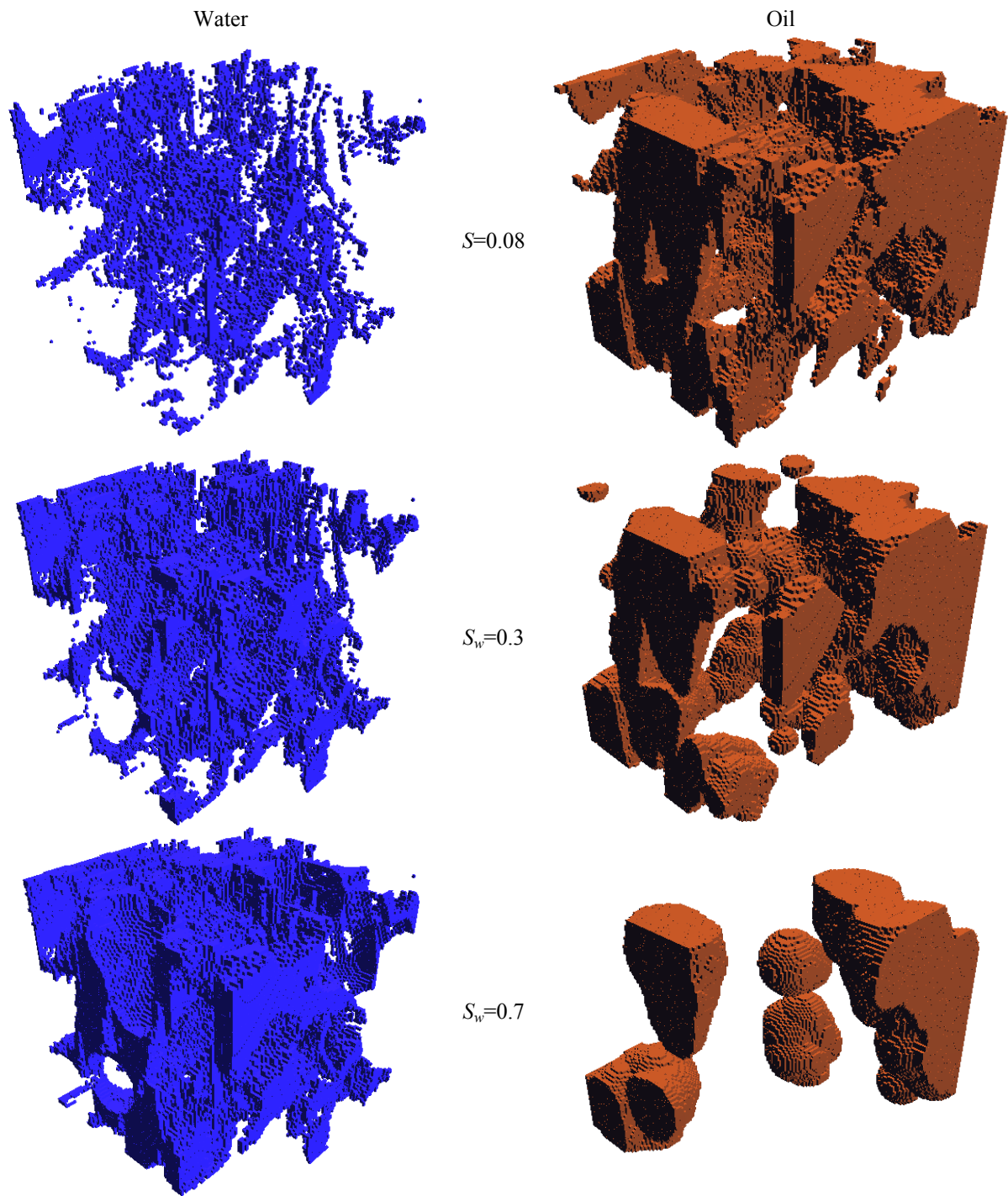
Water   Oil

S=0.08

S_w=0.3

S_w=0.7

Figure 12. Fluid distributions at different saturations in a 100×100×100 voxels fragment. The wetting fluid (left-hand column) has the tendency of occupying the corners and roughness, whereas the nonwetting fluid (right-hand column) is in the central parts of the pores. At S_w=0.3, one observes that the nonwetting fluid is almost disconnected and at S=0.7 the nonwetting fluid separates into disconnected droplets..
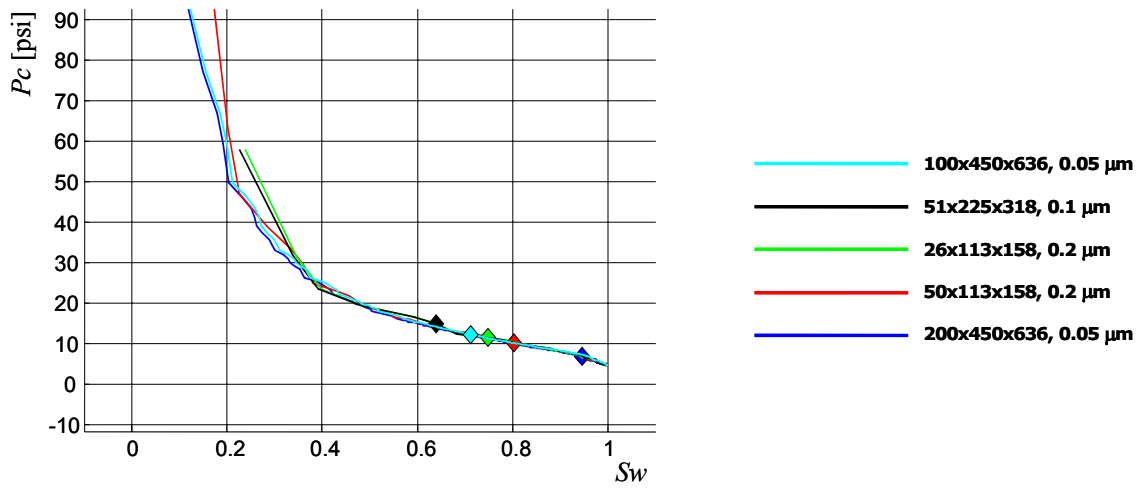
Figure 13. Scaled ordinary-percolation capillary pressure curves computed at different resolutions. The diamonds denote the points where the nonwetting fluid becomes disconnected.
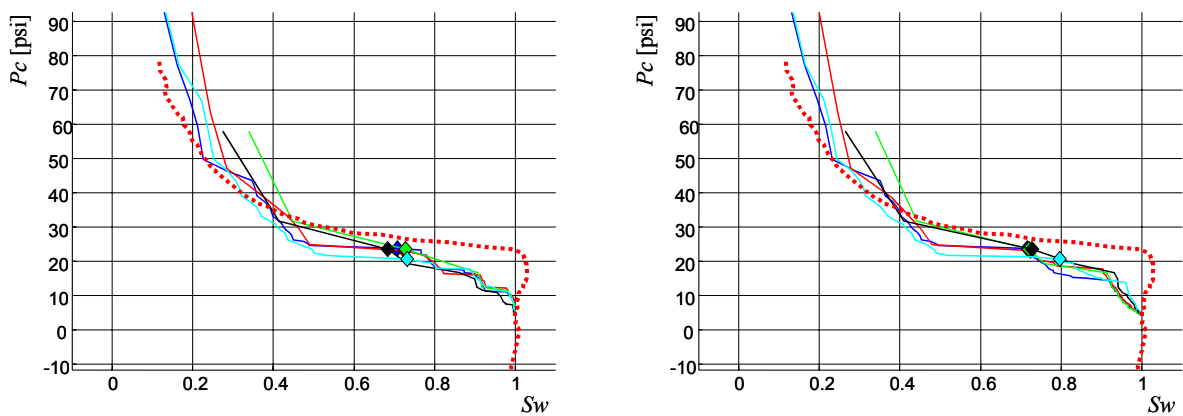

Figure 14. Comparison of scaled invasion-percolation capillary pressure curves in two different directions (solid lines) with experimental drainage capillary pressure curve digitized from Spinler and Baldwin, 1997 (red dotted lines). The diamonds denote the points where the nonwetting fluid becomes disconnected. Different colors denote different resolutions in the same way as in Fig. 13.
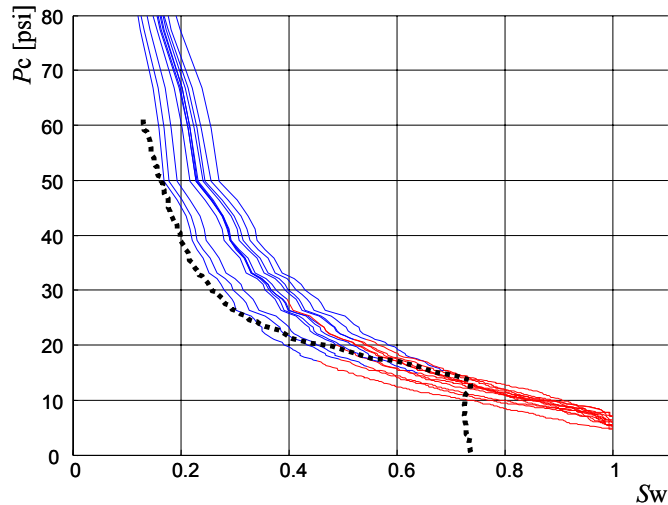
Figure 15. Scaled dimensionless capillary pressure curves (Fig, 11) (solid lines) are plotted together with experimental capillary pressure imbibition curve (black dotted line) digitized from SCA-9705 (Fig. 14).

SUMMARY AND CONCLUSIONS

A new method of sample serial sectioning and imaging using FIB technology has been used to image with submicron resolution the 3D pore structure of chalk. FIB was used to mill successive sample layers as wide as 50 µm and as thin as 0.1µm by sputtering of atoms from the sample surface. Very clean, flat surfaces in which the pore-grain boundaries appear in high contrast have been generated with no apparent distortion of the pore boundaries. The method is suitable to local nanometer scale 3D imaging of selected volumes in large samples.

The nanoscale resolution 3D image of the chalk pore space has been analyzed regarding the pore sizes, equilibrium fluids distribution, and capillary pressure. To process the image, methods described in Silin *et al.*, 2003, 2004 have been applied. The distinctive feature of these methods is that the image of the pore space is analyzed directly, bypassing pore network extraction. The results at high wetting fluid saturation are stable with respect to the image resolution, whereas at low water saturation the image resolution becomes a critical issue. The methods and algorithms used in this study admit modifications to account for mixed wettability, mechanical deformations and damage of the rock and studies of double porosity media.

It has been observed that besides the two orders of the magnitude length scale difference, the chalk images have some qualitative features distinguishing them from sandstone. Most noticeable is the presence of relatively large openings, which manifest themselves as almost horizontal intervals on the drainage capillary pressure curve. There is significant local pore space heterogeneity associated with these larger openings, which makes the appropriate choice of representative imaging sample size a critical issue.

The dimensionless capillary pressure curve provides a signature representation of rock type and can be used as a criterion of success of the computer rock reconstruction. With appropriate scaling, dimensional capillary pressure curves have been generated. Both the shapes of the curves and the absolute values of the pressures are in good agreement with published laboratory data.

ACKNOWLEDGMENTS

REFERENCES

Barenblatt G.I., Patzek T.W., Silin D.B. "The mathematical model of nonequilibrium effects in water-oil displacement", SPE Journal. 8(4):409-416, 2003

Blunt,. M. J. "Flow in porous media - pore-network models and multiphase flow", Current Opinion in Colloid & Interface science, 6(3): 197–207, 2001.

Coles, M.E., Hazlett, R.D., Spanne, P., Soll, W.E., Muegge, E.L., and Jones, K.W., Pore level imaging of fluid transport using synchrotron X-Ray microtomography", SCA9628 Society of Core Analysts Annual Technical Conference, September 8-10, 1996.

Jasty, J.K., Jesion, J., and Feldkamp, L., "Microscopic imaging of porous media with X-ray computed tomography" , SPE Formation Evaluation 189-193, September 1993.

Jin,G., Patzek, T.W. , and D. B. Silin. Physics-based reconstruction of sedimentay rocks. SPE paper 83587 SPE Western Regional/ AAPG Pacific Section Joint Meeting, Long Beach, California, USA, 2003.

Jin,G., Patzek, T.W., and D. B. Silin. Reconstruction of sedimentary rock based on mechanical properties. Physical Review E, Submitted, 2004.

Jin,G., Patzek, T.W., and D. B. Silin, SPE, Direct prediction of the absolute permeability of unconsolidated and consolidated reservoir rock. SPE paper 900084. SPE Annual Technical Conference and Exhibition, Houston, Texas, 2004.

Heaney, P.J., Vicenzi, E.P., Gianuzzi, L.A., and Livi, J.T., Focused Ion Beam Milling: A Method of Site Specific Sample Extraction for Microanalysis of Earth and Planetary Materials," *American Mineralogist*, (2001), **86**, 1094.

Kubis, A.J., G. J. Shiflet, D.N.Dunn and R.Hill, "Focused Ion Beam Tomography", Metalurgical and Material Transactions A, vol. 35A, p. 1935-1943, 2004

Lindquist, W.B.," Quantitative analysis of three dimensional X-ray tomographic images", Development of X-ray Tomography III, U. Bouse (ed), Proceedings of SPIE 4503, 103 SPIE, Bellingham, WA 2002, ftp://ams.sunusb.edu/pub/papers/2001/susb01_06.pdf

Magnani, F. S., P. C. Philippi, Z. R. Liang, and C. P. Fernandes. "Modelling two-phase equilibrium in three-dimensional porous microstructures." International Journal of Multiphase Flow, 26(1): 99–123, 2000.

Mardia, K.V. and T.J.Hainsworth, " A spatial thresholding method for image segmentation" , IEEE Trans. Patt Anal. Mach. Intell. 10(6), pp 919-927, 1988.

Meijering, E. H., W. W. J. Niessen, M. A. Viergever. Quantitative Evaluation of Convolution-Based Methods for Medical Image Interpolation, *Medical Image Analysis*, vol. 5, no. 2, June 2001, pp. 111-126

Muskat. M, Physical principles of oil production McGraw-Hill, 1949

Oh, W., and W.B. Lindquist, "Image thresholding by indicator krigging", IEEE Trans. Patt Anal. Mach. Intell. 21, pp 590-602, 1999.

Øren, Pal-Eric, S. Bakke, and O. J. Arntzen. Extending predictive capabilities to network models. SPE Journal, (December):324–336, 1998.

Øren, Pal-Eric and Stig Bakke. Process based reconstruction of sandstones and prediction of transport properties. Transport in Porous Media, 46(2-3):311–343, 2002.

Orloff, J., L. Swanson, and M. Utlaut, "High Resolution Focused Ion Beams: FIB and Its Applications : The Physics of Liquid Metal Ion Sources and Ion Optics and Their Application to Focused Ion Beam Technology" J, Kluwer Academic Publishers; (November 1, 2002)

Patzek, T. W.. Verification of a complete pore network model of drainage and imbibition. SPEJ, 6(2):144–156, 2001.

Seright, R. S., Liang, J., Lindquist, W.B., and Dunsmuir, J.H., "Use of X-Ray Computed Microtomography to Understand why gels reduce relative permeability to water more than that to oil"., Journal of Petroleum Science and Engineering 39, (2003), pp. 217-230.

Silin, D B. and Tad Patzek. NetSimCPP: Object-Oriented Pore Network Simulator. Lawrence Berkeley National Laboratory, 2001.

Silin, D B. and T. W. Patzek. Object-oriented cluster search for an arbitrary pore network. Technical Report LBNL-51599, Lawrence Berkeley National Laboratory, Berkeley, CA, January 2003.

Silin, D. B., Jin, G., and Patzek, T. W. Robust Determination of the Pore Space Morphology of Sedimentary Rocks. 2003 SPE Paper 84296

Silin, D B., Guodong Jin, and Tad.W. Patzek. Robust Deteremination of the Pore-space Morphology in Sedimentary Rocks. Journal of Petroleum Technology, May: 69–70, 2004.

Silin, D B., Patzek T. On Barenblatt's model of spontaneous countercurrent imbibition. Transport in Porous Media. 54(3):297-322, 2004

Spinler, E. A. and B. A. Baldwin. Capillary pressure scanning curves by direct measurement of saturations. SCA-9705, 1997 International Symposium of the Society of Core Analysts, Calgary, Alberta, Canada, 8_10 September 1997

Stampanoni, M, Borchart, G., Abella, R and P. Ruegsegger, "Bragg Magnifier: A detector for submicrometer x-ray computer tomography", Journal of Applied Physics, (2, no. 12, pp7630-7635, 15 December 2002

Talukdar, M.S., Ioannidis, M., Howard, J., and Torsaeter, O., "Network modeling as a tool for petrophysical measurements in chalk," *Proceedings of the 6th Nordic Symposium on Petrophysics*, (15-16 May 2001), Trondheim, Norway.

Tomutsa, L. and V. Radmilovic, Focused Ion Beam Assisted Three-dimensional Rock Imaging at Submicron Scale, SCA2003-47, 2003 International Symposium of the Society of Core Analysts, Pau, France, 21-24 September 2003.

Wildenschild, D., J.W. Hopmans, C.M.P. Vaz, M.L. Rivers, and D. Rikard, 2002. Using x-ray computed tomography in hydrology: Systems, resolutions, and limitations. Journal of Hydrology, 267(3-4), 285-297.

Xu, B.., J. Kamath, Y. C. Yortsos, and S. H. Lee. Use of pore-network modeling to simulate laboratory corefloods in a heterogeneous carbonate sample. SPE Journa, 4(3): 179-186, 1999.